




# Microenvironment-responsive living hydrogel containing engineered probiotic for treatment of massive bone defects

Haoyu Fang<sup>a,1</sup>, Yanyi Wang<sup>b,c,1</sup>, Li Li<sup>d,e</sup>, Xiaotong Qin<sup>d,e</sup>, Daoyu Zhu<sup>a</sup>, Pei Liu<sup>a</sup>,  
Qianhao Yang<sup>a</sup>, Youshui Gao<sup>a</sup>, Zhongmin Shi<sup>a,\*</sup>, Xin Ma<sup>a,\*\*</sup>, Chao Zhong<sup>b,c,\*\*\*</sup>,  
Yixuan Chen<sup>a,\*\*\*\*</sup> 

<sup>a</sup> Department of Orthopedic Surgery, Shanghai Sixth People's Hospital Affiliated to Shanghai Jiao Tong University School of Medicine, Shanghai, 200233, China

<sup>b</sup> Center for Materials Synthetic Biology, Shenzhen Institute of Synthetic Biology, Shenzhen Institutes of Advanced Technology (SIAT), Chinese Academy of Sciences (CAS), Shenzhen, 518055, China

<sup>c</sup> CAS Key Laboratory of Quantitative Engineering Biology, Shenzhen Institute of Synthetic Biology, Shenzhen Institutes of Advanced Technology (SIAT), Chinese Academy of Sciences (CAS), Shenzhen, 518055, China

<sup>d</sup> State Key Laboratory of Food Nutrition & Safety, Tianjin University of Science & Technology, Tianjin, 300457, China

<sup>e</sup> Key Laboratory of Industrial Fermentation Microbiology (Ministry of Education), Tianjin University of Science & Technology, Tianjin, 300457, China

## ARTICLE INFO

### Keywords:

Living hydrogel  
Bacterial engineering  
Smart biomaterial  
Sensing-reporting  
Regenerative medicine

## ABSTRACT

Self-activating and microenvironment-responsive biomaterials for tissue regeneration would address the escalating need for bone grafting, but remain challenging. The emergence of microbial living therapeutics offers vast potential in regenerative medicine, as genetically engineered probiotics possess efficient stimuli-responsiveness and tunable biological functions. Here, using elevated endogenous nitric oxide (NO) signals as a biological trigger in bone fracture injuries, a Living Responsive Regenerative Medicine (LRRM) strategy for *in situ* bone defect repair through real-time controlled release of bone morphogenetic protein-2 (BMP2) is proposed. The *Escherichia coli* Nissle 1917 (EcN) strain, genetically engineered to sense NO signals and correspondingly produce and secrete BMP2, was firstly encapsulated in gelatin methacryloyl (GelMA) microspheres and then embedded in a bulky hyaluronic acid methacryloyl (HAMA) hydrogel to form a living hydrogel device that circumvents immune attack and prevents bacterial leakage. *In vivo* multiple bone defect models demonstrated the efficacy of the living hydrogel in enhancing the maturation of bone callus, promoting neovascularization, and facilitating full-thickness bone union. Strategic incorporation of engineered probiotics and the bilayer-structured encapsulation system may emerge as an effective and microenvironment-responsive medicine approach for tissue regeneration.

## 1. Introduction

Over the past few decades, increasing research effort has been dedicated to the field of regenerative medicine to address the escalating need for tissue and organ grafting, with various tissue engineering strategies emerging as countermeasures for tissue defects [1–5]. Despite impressive progress, current regenerative medicine approaches often

lack the design considerations of addressing continuous changes in tissue microenvironments, and thus fail to provide self-corrected doses of therapeutics during tissue regeneration. Therefore, the ultimate goal of precise and on-demand tissue regeneration remains as a daunting challenge in the field [5–7].

The microbial living therapeutics exhibits great potential for a wide range of medical applications [8–11], as engineered bacteria can sense

Peer review under the responsibility of editorial board of Bioactive Materials.

\* Corresponding author.

\*\* Corresponding author.

\*\*\* Corresponding author. Center for Materials Synthetic Biology, Shenzhen Institute of Synthetic Biology, Shenzhen Institutes of Advanced Technology (SIAT), Chinese Academy of Sciences (CAS), Shenzhen 518055, China.

\*\*\*\* Corresponding author.

E-mail addresses: [szm1972@sjtu.edu.cn](mailto:szm1972@sjtu.edu.cn) (Z. Shi), [maxin@sjtu.edu.cn](mailto:maxin@sjtu.edu.cn) (X. Ma), [chao.zhong@siat.ac.cn](mailto:chao.zhong@siat.ac.cn) (C. Zhong), [cyxwlp0987@alumni.sjtu.edu.cn](mailto:cyxwlp0987@alumni.sjtu.edu.cn) (Y. Chen).

<sup>1</sup> These authors contributed equally to this work.

<https://doi.org/10.1016/j.bioactmat.2025.04.020>

Received 6 November 2024; Received in revised form 2 April 2025; Accepted 16 April 2025

2452-199X/© 2025 The Authors. Publishing services by Elsevier B.V. on behalf of KeAi Communications Co. Ltd. This is an open access article under the CC BY-NC-ND license (<http://creativecommons.org/licenses/by-nc-nd/4.0/>).

minute amounts of microenvironmental signals, perform computations based on these signals, and modulate specific parameters in response. For example, bacteria have been successfully programmed to detect physical and chemical signals such as light, ultrasound, temperature, and some chemical molecules. This intriguing property has inspired scientists to engineer bacteria that can sense disease markers, thereby paving the way for disease diagnosis and precise drug delivery. For biosafety considerations, the Generally Recognized as Safe (GRAS) species of bacteria were preferred, including *E. coli* Nissle 1917 (EcN) [12], *Lactococcus lactis* [13], and *Saccharomyces cerevisiae* [14]. To date, there are only a few disease markers for which responsive genetic circuits have been developed for probiotics, mainly including those for glucose [15], blood [16], tetrathionate [17], and nitric oxide (NO) [18]. By combining these biosensing circuits with fluorescent proteins as the output signals, these beneficial bacteria can be designed for disease diagnosis. Another attractive feature of microbial living therapeutics is that the bacteria can be programmed to secrete proteins or small molecules for therapeutic purposes, including cytokines (TFF3) for inflammatory bowel disease (IBD) treatment [12], vascular endothelial growth factor (VEGF) for diabetic wound healing [19], and anti-cancer agents (Toll-like receptor 5 agonists) for cancer intervention [20]. These smart whole-cell devices release drugs *in situ* in a self-regulating manner to enable timely treatment, making them attractive for the treatment of complex and persistent diseases [21]. Despite these advances in microbial living therapeutics, few signaling molecules have been exploited to sense the bone healing process, and the application of such strategies in deep tissue regeneration, such as bone regeneration, remains largely unexplored.

Impaired bone healing and regeneration are significant challenges associated with severe trauma, and the management of massive bone defects remains a critical therapeutic challenge. Over the past few decades, implantation of functional biomaterials has emerged as a common strategy for treating massive bone defects [22–25]. Recently, therapeutic approaches using synthetic bone-graft substitutes and osteoinductive factors have shown significant promise. Specifically,

bone morphogenetic protein 2 (BMP2) has demonstrated therapeutic potential in the treatment of bone defects over the past few decades [26–28]. Unfortunately, the short half-life and burst release of BMP2 in conventional controlled-release systems limit its clinical application. The burst release of BMP2 poses additional concerns, including complications associated with ectopic bone formation, failure of vascularization [29–31], and increased risk of cancer development [32,33]. Therefore, there is an urgent need to develop a self-activating and microenvironment-responsive therapeutic approach that can spontaneously respond to the microenvironment with high efficiency and accelerate new bone formation to meet clinical demands.

Herein, inspired by the finding that the endogenous NO concentration increases following bone injury, we report a Living Responsive Regenerative Medicine (LRRM) strategy for highly efficient bone defect repair through real-time NO-responsiveness and *in situ* release of BMP2. Using an artificial NO-inducible gene circuit, we genetically engineered the EcN strain to sense NO signals and correspondingly respond to express and secrete BMP2. The engineered probiotics were subsequently encapsulated in gelatin methacryloyl (GelMA) hydrogel microspheres and then embedded in a bulky hyaluronic acid methacryloyl (HAMA) hydrogel network, resulting in a bilayer-structured living hydrogel device that circumvents immune attack and prevents bacterial leakage. When implanted into mouse models with cranial or femoral bone defects, the living hydrogel, triggered by elevated endogenous NO at the fracture site, could produce BMP2 *in situ* and thus promote bone union in a controlled manner (Fig. 1). Our study demonstrated the potential of microbial living therapeutics for the treatment of massive bone defects. We anticipate that this type of smart living hydrogel with a biological signal-eliciting functional response system will provide an alternative regenerative medicine solution characterized by excellent microenvironmental responsiveness and tunable biological-functionality.

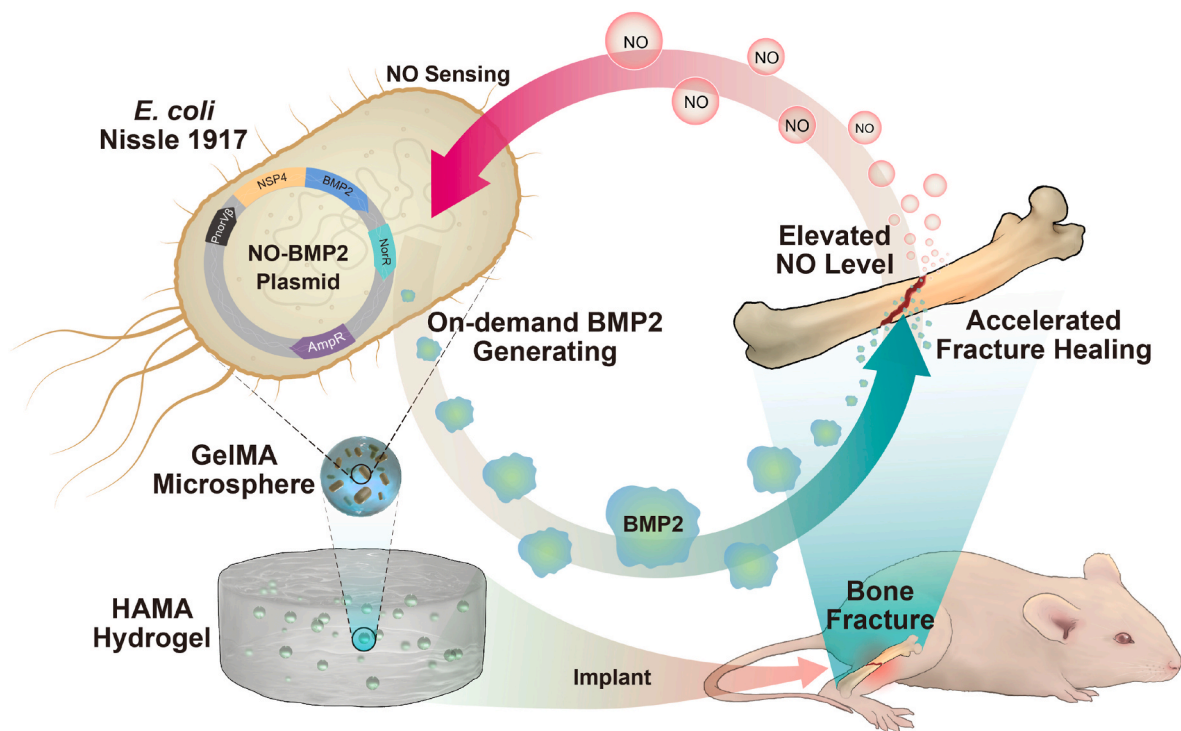


**Fig. 1.** Schematic illustration of the fabrication process and the bone healing promotion capability of the living hydrogel. The engineered smart living hydrogel features sensitive NO detection, self-regulated BMP2 secretion, and bone regeneration stimulation, providing high-efficient therapeutic countermeasure for fracture healing and bone regeneration.

## 2. Materials and methods

### 2.1. Bacterial strains and culture conditions

All genetic manipulations were conducted on *Escherichia coli* Nissle 1917 strains and sequenced. Once verified, the constructs were then electroporated into EcN competent cells under optimized parameters (1.8 kV, 6 ms) for protein expression and animal experiments. Both the *E. coli* and EcN strains were cultured in lysogeny broth (LB) media (Solarbio, Beijing, China) supplemented with the appropriate antibiotics at 37 °C.

### 2.2. Plasmid and strain construction

To construct a plasmid for NO-induced fluorescent protein expression, we constructed the pET22b-PnorV $\beta$ -norR-gfp plasmid. Briefly, the gene fragments of the PnorV $\beta$  promoter and NorR regulator were synthesized by GENEWIZ, and the *gfp* gene sequence from the plasmid available in our lab was amplified. These three gene fragments were then inserted into the linearized pET22b backbone using the one-step Gibson assembly method, resulting in the formation of pET22b-PnorV $\beta$ -norR-gfp.

To construct a plasmid for NO-induced BMP2 protein secretion, we constructed the pET22b-PnorV $\beta$ -norR-NSP4-bmp2 plasmid. Our strategy for constructing this target plasmid involved replacing the *gfp* gene in the pET22b-PnorV $\beta$ -norR-gfp plasmid with the gene sequence of NSP4-BMP2. The gene fragment of the NSP4-BMP2 fusion protein synthesized by GENEWIZ was amplified to carry the homology arms, and then assembled with the linearized vector to form pET22b-PnorV $\beta$ -norR-NSP4-bmp2.

The pET22b-PnorV $\beta$ -norR-gfp plasmid was transformed into the EcN strain to generate the EcN\_GFP strain. The pET22b-PnorV $\beta$ -norR-NSP4-bmp2 plasmid was transformed into the EcN strain to generate the EcN\_BMP2 strain. Unless otherwise specified, the wild EcN strain was cultured in antibiotic-free LB medium, while the EcN-GFP and EcN-BMP2 strains were cultured in the LB medium supplemented with 100  $\mu$ g/mL of carbenicillin.

### 2.3. NO induction and time kinetic experiment

The EcN and EcN\_GFP strains were initially inoculated from glycerol stocks into the LB medium and cultured for 16 h at 37 °C, 220 rpm. Overnight bacterial cultures were concentrated and reinoculated into the fresh LB medium at an optical density (OD) of 0.1. To monitor the protein expression level of the EcN\_GFP strain at different inducer concentrations, a gradient concentration (0, 50, 100, 200, 400, 600, 800, and 1000  $\mu$ M) of DETA-NONOate was added to 1 mL of bacterial-containing medium and incubated for 24 h. The fluorescence intensity was quantified using a microplate reader (Tecan Infinite® 200pro, Männedorf, Switzerland). To record the induction kinetics of the EcN\_GFP strain, 1000  $\mu$ M of DETA-NONOate was added to 1 mL of bacterial-containing medium and incubated for 48 h. The fluorescence intensity was measured at 2-h intervals for the first 12 h and at 6-h intervals thereafter. Microscopic images were captured using a confocal laser scanning microscope (CLSM; Nikon AX, Tokyo, Japan).

### 2.4. Verification of NO-induced BMP2 expression in the EcN\_BMP2 strain

Wild-type EcN and EcN\_BMP2 strains were incubated overnight. Then, the saturated bacterial solution was inoculated into the fresh LB medium supplemented with 1000  $\mu$ M of DETA-NONOate at a ratio of 1:100. After 24-h of incubation at 37 °C, the bacterial solution was centrifuged to isolate the bacteria and supernatant. To verify the presence of BMP2, 1 mL of the culture supernatant was concentrated 10-fold by precipitation with trichloroacetic acid and analyzed by western blotting using an anti-His antibody. To monitor the secretion amount of

BMP2, the culture supernatants were assayed using a His-tag ELISA Detection Kit (GenScript, Nanjing, China).

### 2.5. Preparation of EcN-loaded hydrogels

To prepare the EcN@GelMA@HAMA composite hydrogels, the EcN strain was first encapsulated in GelMA microspheres and then embedded within a HAMA matrix. Briefly, GelMA powder (2.5 % w/v) and lithium phenyl-2,4,6-trimethylbenzoylphosphinate (LAP, 0.15 % w/v) were dissolved in 1 mL of LB medium to prepare the GelMA precursor solution. An overnight culture of EcN was resuspended in this solution to achieve a final OD of 1, and the EcN-containing precursor solution was used to fabricate microspheres using a microfluidic device (FluidicLAB, Shanghai, China). The droplets, dispersed in microfluidic oil, were photo-crosslinked under UV light for 30 s, then sequentially washed with acetone and PBS, and stored in PBS until use.

Separately, HAMA powder (3 % w/v) and LAP (0.15 % w/v) were dissolved in 1 mL LB medium to prepare the HAMA precursor solution. The GelMA microspheres were gently mixed with the HAMA precursor at a 1:1 vol ratio, and 250  $\mu$ L of the mixture was injected into a cylindrical silicone mold (6 mm diameter). The hydrogel was then photo-crosslinked under UV light for an additional 30 s, forming a composite hydrogel with a final bacterial OD of 0.5.

To prepare EcN@HAMA hydrogels, the overnight EcN culture was directly resuspended in the HAMA precursor (3 % w/v HAMA, 0.15 % w/v LAP) to achieve a final bacterial OD of 0.5. The solution was injected into the same cylindrical silicone mold (6 mm diameter) and photo-crosslinked for 30 s, yielding EcN@HAMA hydrogels. All prepared hydrogels were temporarily stored in PBS for subsequent experiments. Based on colony counting of a 1 OD EcN culture, we estimated that each cylindrical hydrogel (6 mm diameter) contained approximately  $1.2 \times 10^9$  CFU of EcN.

### 2.6. Assessment of BMP2 release from living hydrogels

To assess the NO-responsive production and release of BMP2 by the engineered bacteria encapsulated within the hydrogel, we fabricated EcN-loaded composite hydrogels using the EcN\_BMP2 strain following the protocol detailed in “2.5. Preparation of EcN-loaded hydrogels”. The resulting living hydrogels were immersed in 1 mL of PBS with or without 1-mM DETA-NONOate (NO donor) and incubated at 37 °C. Supernatant samples were collected at 24, 48, and 72 h for BMP2 quantification. To maintain a constant volume, an equal amount of fresh PBS was added immediately after each sampling. BMP2 concentration was measured using a His-tag ELISA Detection Kit (GenScript, Nanjing, China) according to the manufacturer’s protocol. Absorbance was measured at 450 nm using a microplate reader (Tecan Infinite® 200pro, Männedorf, Switzerland).

### 2.7. Microspheres size analysis

To analyze the microsphere size distribution, an appropriate quantity of EcN@GelMA microspheres in the oil phase was transferred to a standard glass-bottom dish. Five images were captured using CLSM in an optical channel. A total of 100 microspheres were analyzed using the Image Pro Plus software.

### 2.8. Morphological characterization of EcN-loaded hydrogels

The obtained EcN@GelMA microspheres and EcN@GelMA@HAMA hydrogels were refrigerated at –20 °C overnight and subsequently freeze-dried for 2 days in a lyophilizer (Scientz-12ND, Ningbo, China). To prepare the samples for SEM imaging, they were coated with gold and imaged using the Phenom Pharos G2 (Phenom, Netherlands).

## 2.9. Bacterial viability assessment

EcN-containing hydrogels were incubated in 1 mL of PBS at an incubation temperature of 37 °C. The bacterial viability was assessed using a live/dead assay (Thermo Fisher Scientific, Waltham, MA, USA) at designated time points (days 1, 3, 5, 7, and 10 post-encapsulation). The live/dead staining solution was freshly prepared by adding 1 µL of SYTO9 and 1 µL of PI to 200 µL of PBS. The hydrogels loaded with EcN were stained with 200 µL of the dye solution. After 15-min incubation in the dark, the hydrogels were rinsed three times with PBS to remove excess fluorescent dye and imaged using CLSM (Nikon AX, Tokyo, Japan).

## 2.10. Bacterial leakage test

The prepared EcN-containing hydrogels (EcN @GelMA@HAMA and EcN @HAMA) were immersed in PBS and incubated at 37 °C in an incubator for 48 h. After incubation, the soaked supernatants were diluted 10-fold and spread onto LB agar plates. After overnight growth, digital images of the LB agar plates were captured, and the number of leaked bacteria was counted using Image Pro Plus software.

## 2.11. Cell culture and in vitro cytotoxicity assay

Human bone marrow mesenchymal stem cells (BMSCs) were purchased from the Cell Bank of the Chinese Academy of Sciences (Shanghai, China). The BMSCs were cultured in the Minimum Essential Medium Alpha (α-MEM) (Gibco BRL, Grand Island, NY, USA), supplemented with 10 % of fetal bovine serum (FBS) (Gibco BRL) and 100 mg/mL of penicillin and streptomycin (Gibco BRL). The cells were cultured in the cell incubator with a humidified atmosphere of 5 % CO<sub>2</sub> at 37 °C. Cell proliferation was assessed using the Cell Counting Kit-8 (CCK-8) (Dojindo, Kumamoto, Japan). Cells were seeded at a density of  $2.5 \times 10^3$  per well in a 96-well plate. After co-culture with the soaked supernatant from different groups of hydrogels respectively for predetermined time intervals, the CCK-8 solution was added into each well and incubated for 2 h. The absorbance of each well was measured using Varioskan LUX (Thermo Fisher Scientific, Waltham, MA, USA). To examine the biocompatibility of different hydrogels, live/dead cell staining was carried out using the Calcein/PI live/dead viability/cytotoxicity assay kit (Beyotime, Shanghai, China). Furthermore, BMSCs co-cultured with different hydrogels were stained with rhodamine phalloidin and Hoechst 33342 to further observe subtle cytoskeletal changes using a DMi8 inverted microscope (Leica, Wetzlar, Germany).

## 2.12. Quantitative real-time polymerase chain reaction (RT-qPCR)

Total mRNA was extracted from BMSCs using the EZBioscience EZpress RNA purification kit B0004DP (EZBioscience, Roseville, MN, USA). The RT-PCR reaction system was prepared with the EZBioscience 2 × Color SYBR Green qPCR Master Mix (ROX2 plus) A0012-R2 (EZBioscience, Roseville, MN, USA). In brief, 5 µL of Color SYBR Green qPCR Master Mix, 0.2 µL of upstream primers, 0.2 µL of downstream primers, 4 µL of cDNA, and 0.6 µL of ddH<sub>2</sub>O were added into the reaction system. Subsequently, RT-qPCR was conducted on an ABI 7900 HT Sequence Detection System (Thermo Fisher Scientific, Waltham, MA, USA).

## 2.13. Osteogenic differentiation, alizarin red staining (ARS) and alkaline phosphatase staining (ALP)

The osteogenic differentiation medium was prepared by adding 50 µg/mL of ascorbic acid (Sigma-Aldrich, St. Louis, MO, USA), 10 mmol/L of β-glycerophosphate (Sigma-Aldrich), and 10 nmol/L of dexamethasone (Sigma-Aldrich) into the culture medium described earlier. BMSCs were seeded in a 48-well plate and cultured in an osteogenic

differentiation medium at predetermined time intervals. After a 14-day co-culture with different hydrogels, BMSCs were washed three times with PBS before being fixed with 4 % paraformaldehyde solution and subsequently stained using the BCIP/NBT alkaline phosphatase color development kit (Beyotime, Shanghai, China). After a 21-day co-culture with different hydrogels, BMSCs were washed three times with PBS before being fixed with 4 % paraformaldehyde, and subsequently stained with 2 % Alizarin Red S staining solution (Beyotime, Shanghai, China). Images were captured using the Leica SAPO light microscope (Leica, Wetzlar, Germany) and corresponding imaging system (Leica MC190 HD, Wetzlar, Germany). Quantification was performed using the Image Pro Plus software.

## 2.14. Modeling of femoral shaft fracture

A total of 30 male C57BL/6 mice weighing approximately 25 g were utilized for the femoral shaft defect model. All procedures for the care and use of laboratory animals were approved by the Animal Research Committee of Shanghai Sixth People's Hospital Affiliated to Shanghai Jiao Tong University School of Medicine (No. 2023–0204). The mice were randomized into three groups: (1) Control Hydrogel (Ctrl@H) group (N = 10), (2) Nissle 1917 Hydrogel (EcN@H) group (N = 10), and (3) EcN\_BMP2 Hydrogel (mEcN@H) group (N = 10). After anesthetizing the mice by isoflurane inhalation, the area near the left hind limb was shaved and disinfected. A small incision approximately 1 cm in length was made along the dorsal skin of the distal femur. The muscle gap was bluntly separated to expose the mid-shaft of the femur. Then, a 26-gauge needle was slowly inserted from the distal end of the femur into the intramedullary canal until the needle tip reached the end of the femoral medullary cavity. Subsequently, a transverse segmental bone defect around 1 mm in diameter is made in the midshaft of femur using a dental drill, as previously described [34]. During the operation, the femur was continuously rinsed with a large amount of saline to prevent the hyperthermal effect on the surrounding bone. Designated hydrogels (Φ3 mm × 1 mm) were inserted into fracture sites. After confirming the stability of the needle in the medullary cavity, the needle tip was cut off, and the wound was carefully sutured layer by layer. These mice were sacrificed at different time points (Day 14 and Day 28), and the fractured femurs were harvested. No signs of infection or any other complications were observed in any mice. All mice were included in the data analysis.

## 2.15. Modeling of cranial defect

A total of 30 male C57BL/6 mice weighing approximately 25 g were utilized for the cranial defect model. All procedures for the care and use of laboratory animals were approved by the Animal Research Committee of Shanghai Sixth People's Hospital Affiliated to Shanghai Jiao Tong University School of Medicine (No. 2023–0204). These mice were randomized into three groups: (1) Control Hydrogel (Ctrl@H) group (N = 10), (2) Nissle 1917 Hydrogel (EcN@H) group (N = 10), and (3) EcN\_BMP2 Hydrogel (mEcN@H) group (N = 10). After anesthetizing the mice by isoflurane inhalation, the area near the cranium was shaved and disinfected. A small incision, approximately 1 cm in length, was made directly above the cranium. Two 3-mm cranial defects were created by an electric trephine (Nouvag AG, Goldach, Switzerland) under low-speed drilling, which were subsequently implanted with the indicated hydrogels (Φ3 mm × 1 mm), respectively. During the operation, the cranium was continuously rinsed with a large amount of saline to prevent the hyperthermal effect on the surrounding bone. Then the wound was carefully sutured. The animals were sacrificed at different time points (Day 14 and Day 28), and the craniums were harvested. No signs of infection or any other complications were observed in any mice. All mice were included in the data analysis.



## 2.16. Radiographic imaging

For the femoral shaft defect models and cranial defect models, five mice were randomly selected from each group at 14 and 28 days after surgery, respectively. Following anesthesia by isoflurane inhalation, plain radiographic images of the femurs were acquired using a Faxitron X-ray MX-20 Specimen Radiography System (Tucson, AZ, USA).

## 2.17. Micro-computed tomography (micro-CT) imaging

The harvested craniums and femurs were submerged in the 4 % paraformaldehyde solution overnight. Micro-CT was performed using a micro-CT scanner (Bruker Skyscan 1176, Kontich, Belgium) with a voxel size of 9  $\mu\text{m}$ . The acquired data were then reconstructed using the CTvox and Mimics software. Bone mineral density (BMD), bone volume/total volume (BV/TV), total porosity and trabecular number (Tb.N) were measured using the DataViewer and CTan software. (Thresholding value: 65. Volume of interest: For the mouse femoral shaft fracture model, callus tissue within 1 mm region on both sides of the fracture line was uniformly defined as the area for analysis; For the mouse cranial defect model, the original defected region ( $\Phi 3$  mm) was uniformly defined as the area for analysis).

## 2.18. Histologic and immunohistochemical analyses

After micro-CT scanning, the harvested specimens were decalcified using 10 % ethylenediaminetetraacetic acid solution for a duration of 2 weeks. The specimens underwent the embedment in paraffin before sliced into sections with a thickness of 5  $\mu\text{m}$ . Morphological staining, including hematoxylin and eosin (H&E) staining and Safranin-O/Fast Green staining, was subsequently carried out. The resulting images were captured using a Leica DM4000 microscope (Leica, Wetzlar, Germany).

Immunohistochemical staining was carried out on the slices to identify the expression of several biomolecules, including RUNX family transcription factor 2 (RUNX2), collagen type I (COL1), matrix metalloproteinases-13 (MMP13), platelet endothelial cell adhesion molecule-1 (PECAM-1/CD31), and vascular endothelial growth factor (VEGF). Antibodies for RUNX2, COL1, MMP13, CD31, and VEGF were purchased from Abcam (Cambridge, UK). The images of immunohistochemical staining were captured using a 3DHISTECH Panoramic MIDI (3DHISTECH Ltd., Budapest, Hungary). The proportion of positive staining areas in each immunohistochemical staining image was analyzed and calculated using Image Pro Plus software (Region of interest: For the mouse femoral shaft fracture model, callus tissue within 1 mm region on both sides of the fracture line was uniformly defined as the area for analysis; For the mouse cranial defect model, the original defected region ( $\Phi 3$  mm) was uniformly defined as the area for analysis).

## 2.19. Statistical analysis

Statistical analysis was performed using Stata 15 software. All data were expressed as mean  $\pm$  standard deviation from at least three replicates. To assess the significant differences between two groups, the Unpaired Student's t-test was utilized. For multiple comparisons, the one-way analysis of variance or two-way analysis of variance was conducted. The assumptions of normality and homogeneity of variance were verified using the Shapiro-Wilk test and Bartlett's test, respectively. A  $p$ -value of  $\geq 0.05$  indicated no statistical significance, denoted as "ns". A  $p$ -value of  $< 0.05$  indicated statistical significance, denoted as "\*\*". A  $p$ -value of  $< 0.01$  indicated moderately significant statistical difference, denoted as "\*\*\*". A  $p$ -value of  $< 0.001$  indicated highly significant statistical difference, denoted as "\*\*\*\*".

## 3. Results

### 3.1. Construction of NO-responsive EcN strain

Previous studies have revealed that NO synthase is activated during bone fracture, leading to elevated serum NO levels along with the body's self-repair process [35–39]. Recent studies have shown that serum NO levels increase after the femoral fracture, reaching a peak between 7 and 14 days post-injury, and then decreases by day 28 [37]. Our previous work emphasized that a critical period of 7–14 days marks the initiation of natural bone healing, and day 28 is the time point of final bone union in mice [40]. Given these findings, NO may emerge as an ideal trigger for the controlled release of BMP2 required for bone healing. This approach would reduce the risks of insufficient release and excessive release, thereby optimizing the healing process.

Among the existing transcriptional NO-sensing pathways, the PnorV $\beta$  promoter and its NorR regulator are preferred for biomedical applications because of their high sensitivity ( $\sim$ nM, far below physiological concentrations) and superior specificity. We used EcN as our cellular chassis because of its long safety record in humans and compatibility with canonical genetic engineering techniques for bacteria. To verify the feasibility of this regulatory system in EcN cells, we created plasmid-based genetic constructs by placing green fluorescent protein (GFP) under the control of the PnorV $\beta$  promoter. The NorR gene is also regulated by the PnorV $\beta$  promoter, creating a positive feedback loop capable of fine-tuning NorR expression levels, leading to greater induction and higher amplitude [41] (Fig. 2A). The pET22b-PnorV $\beta$ -norR-gfp plasmid was subsequently transformed into the EcN strain to form a new strain that can sense minute amount of NO, abbreviated as the EcN\_GFP strain.

In our *in vitro* experiments, we used DETA-NONOate, which has a half-life of approximately 20 h, as the NO donor. Higher concentrations of the donor released more NO into the lysogeny broth (LB) medium, with the 1-mM donor releasing approximately 260- $\mu\text{M}$  NO, similar to concentrations at bone fracture sites (Fig. 2B). We evaluated the engineered EcN strain response by measuring the fluorescence intensity, which correlated positively with the inducer concentration (Fig. 2C). Confocal laser scanning microscopy (CLSM) confirmed that the bacteria fluoresced green only in the presence of the NO donor (Fig. 2D). The induction kinetics showed a sensitive NO response, with protein expression peaking at approximately 12 h (Fig. 2E).

To achieve the goal of engineering probiotics for bone regeneration, we genetically modified EcN by transforming a plasmid encoding BMP2, an acclaimed growth differentiation factor that not only stimulates osteoblast differentiation, but also plays a necessary role in the signaling cascade that governs fracture repair [42] (Fig. 2F). The expression of the *bmp2* gene was driven by the inducible promoter PnorV $\beta$ , and fused with an NSP4 signal peptide for secretion and a His-tag for detection. The resulting plasmid, pET22b-PnorV $\beta$ -norR-NSP4-bmp2, was transformed into EcN to create the NO-induced BMP2-secreting strain (abbreviated as the EcN\_BMP2 strain). Western blot analysis using an anti-His antibody confirmed BMP2 secretion into the culture medium, with wild-type EcN as a control (Fig. 2G). ELISA also confirmed the presence of BMP2 in the supernatant, showing that 1-mM NO donor maximized BMP2 production ( $\approx 11.15$  ng/mL) after 24 h (Fig. 2H). Thus, we successfully constructed a strain sensitive to NO and capable of producing BMP2.

### 3.2. Preparation and characterization of probiotic-loaded living hydrogel

To prevent bacterial leakage, a double-layered composite hydrogel (GelMA@HAMA) system with superior biocompatibility was selected [43]. Fig. 3A depicts the efficient preparation of the EcN@GelMA@HAMA composite material in two steps: engineered EcN was first encapsulated into GelMA hydrogel microspheres using a microfluidic chip and then covalently crosslinked through photo-crosslinking. Next, the obtained bacteria-containing microspheres were embedded in bulk

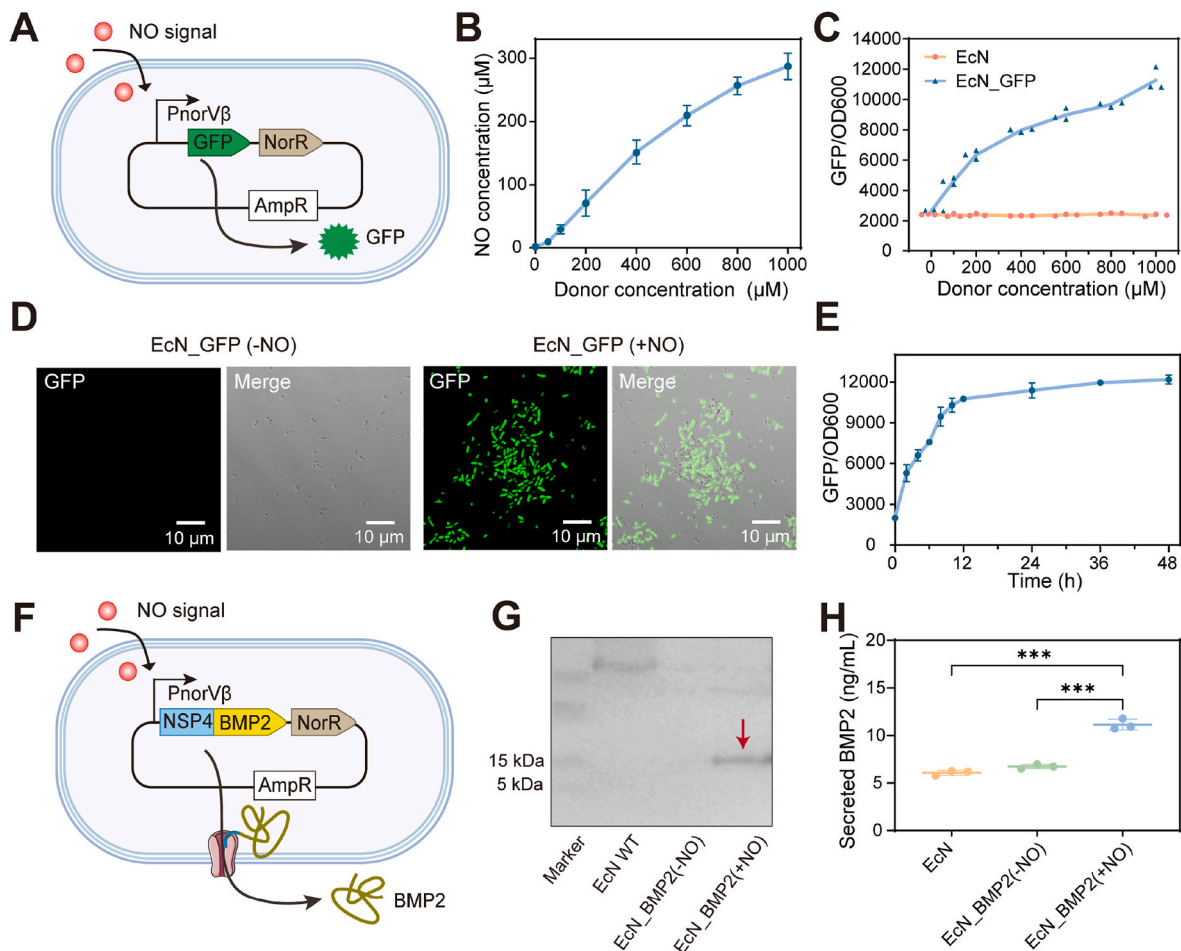


**Fig. 2.** Construction and performance assessment of the NO-responsive engineered EcN strains. (A) Schematic diagram of the engineered strain containing the artificial NO-inducible gene circuits for NO-induced expression of GFP, which serves as a reporter protein, put under the control of the NO-inducible *P<sub>norVβ</sub>* promoter. (B) Determination of NO in solutions released by different concentrations of DETA-NONOate. DETA-NONOate gradients used are 0, 50, 100, 200, 400, 600, 800, and 1000 μM. (C) The GFP expression levels in the NO sensor (EcN\_GFP) strains at various NO donor concentrations. (D) GFP fluorescence of EcN\_GFP strains with and without the addition of NO donor recorded by confocal laser scanning microscopy (CLSM). In the absence of NO donor, green fluorescence was not observed in the bacteria. (E) Induction kinetics of the NorR-based regulatory circuits in EcN under 1000 μM NO donor. (F) Schematic diagram of the modified construct for secreted expression of BMP2 after sensing NO stimulation. (G) Detection of the BMP2 protein in the supernatant by Western blot. (H) BMP2 secreted by EcN strains after 24 h of incubation was quantified using ELISA. If not otherwise specified, the NO donor was used at a concentration of 1000 μM. (All data points represent mean  $\pm$  standard deviation of three independent replicates. Statistics were derived using the one-way analysis of variance. \*\*\**P* < 0.001.)

HAMA hydrogels using a second photo-crosslinking process. To visualize the successful encapsulation of bacteria in the hydrogel microspheres in step 1, we used EcN constitutively expressing GFP. CLSM images confirmed effective encasement of bacteria in the microspheres (Fig. 3B), with an average diameter of 100 μm as determined using the Image Pro Plus software (Fig. 3C). Scanning electron microscopy (SEM) images showed an irregular porous structure on the surface of the lyophilized EcN@GelMA microspheres (Fig. 3D). After photo-crosslinking in 6-mm silicone molds, the resulting EcN@GelMA@HAMA composite hydrogels appeared slightly cloudy owing to bacterial containment (Fig. 3E). Cross-sectional SEM images showed porous microspheres consistent with lyophilized microspheres (Fig. 3F).

We incubated the hydrogels in simulated body fluid (SBF) for 7 days to further assess the survival of bacteria in the hydrogels. CLSM images were recorded at different time points after staining using live/dead kits. The bacteria remained viable until day 7, indicating that the hydrogel did not cause significant harm. However, owing to nutrient depletion, the bacteria began to die by day 10 (Fig. 3G). As mentioned above, another important function of hydrogel scaffolding is to create a physical barrier and prevent bacteria from escaping. Therefore, we examined their protective effects by counting the number of bacteria in the

solution after immersion, using a plate-counting method. Bacteria directly encapsulated in HAMA hydrogel were used as controls. Numerous EcN colonies were observed on the plates of the EcN@HAMA hydrogel group, whereas no bacterial growth was observed on the plates of the EcN@GelMA@HAMA group (Fig. 3H, Fig. S1). Quantitative analysis revealed that the percentage of bacterial leakage in the EcN@HAMA hydrogel group was 6.3 %. These results confirmed that the EcN@GelMA@HAMA hydrogels possess a favorable biosafety profile to avoid potential bacterial infections, thus offering a promising platform for living bacterial therapy.

### 3.3. The sensing-reporting capacity of the smart living hydrogel

It is widely acknowledged that nascent blood vessels recruited in the soft callus initiate coupled remodeling and mineralization of the cartilaginous callus at the early stage (that is, day 5–10) of long bone fracture healing [44]. Neovascularization is initiated immediately after fracture occurrence and peaks at day 7, whereas the ossification and mineralization phases are subsequently initiated 3 days after fracture and predominate from day 14 to the later stage of fracture repair [45]. To corroborate these findings, we established a mouse femoral fracture

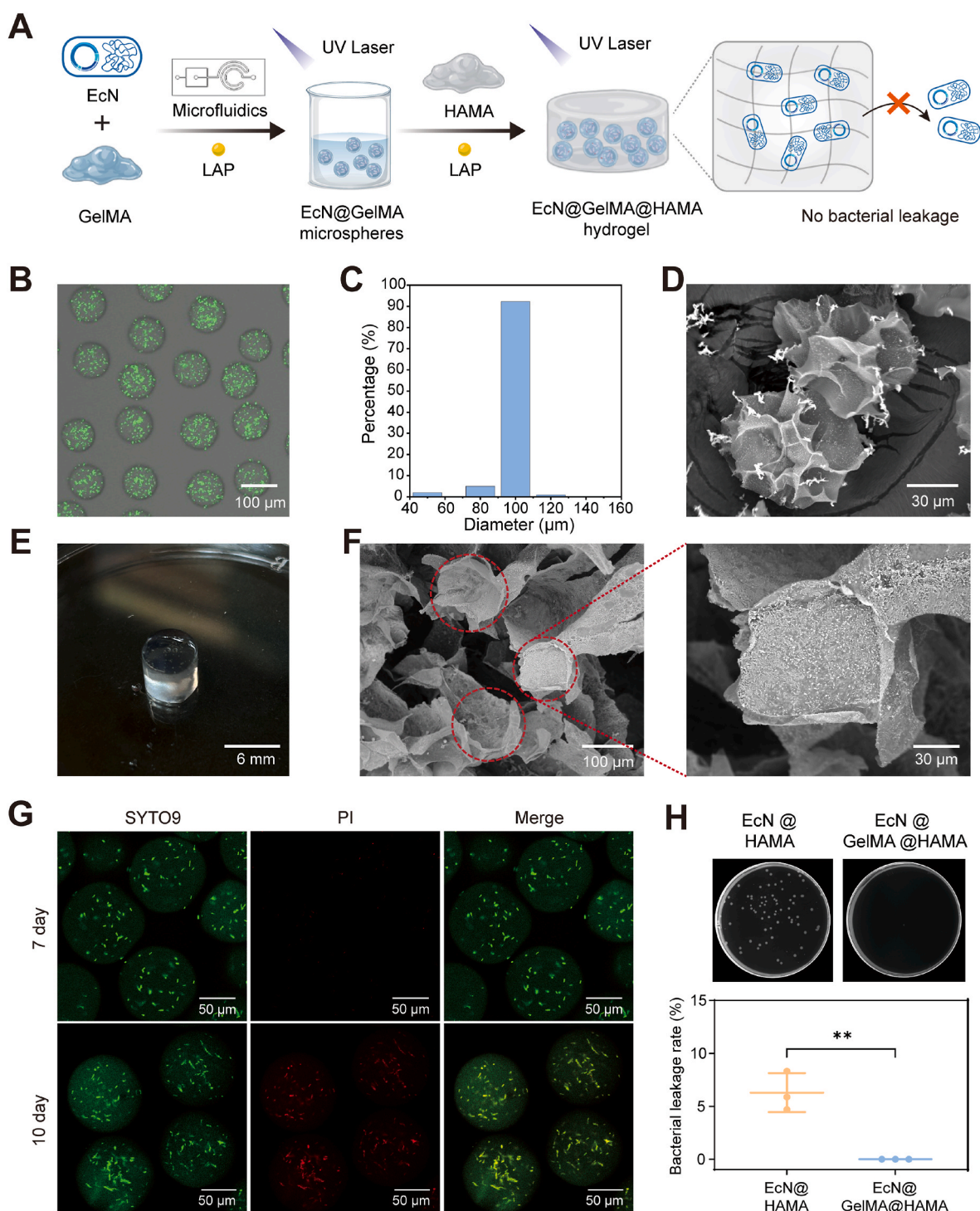


**Fig. 3.** Preparation and characterization of the probiotic-enabled living hydrogel. (A) Schematic illustration depicting the fabrication process of living hydrogel device. First, the engineered bacteria were gently mixed with 2.5 % (w/v) GelMA to prepare a 1 OD bacteria suspension as precursor solution, which was then processed into bacteria-laden microspheres using a microfluidic device. Next, the bacteria-laden microspheres were mixed with 3 % (w/v) HAMA to obtain a bulk hydrogel material. In both steps, the curing of the hydrogels was accomplished by photocrosslinking. (B) Representative images of EcN@GelMA microspheres. (C) Size distribution histograms of EcN@GelMA microspheres. (D) SEM images of EcN@GelMA microspheres. (E) Digital image of prepared EcN@GelMA@HAMA living hydrogel. (F) SEM images of EcN@GelMA@HAMA living hydrogel. Samples were freeze-dried before observation. (G) Live-dead staining experiments to explore the survival of bacteria in hydrogels. (Live: SYTO9, green; Dead: PI, red.) (H) Bacterial leakage test examines the ability of GelMA/HAMA hydrogels to prevent bacterial escape after 48 h incubation. The leakage ratio for HAMA hydrogel and GelMA/HAMA hydrogel was 6.3 % and 0 %, respectively. The images above the bar graph show colonies that proliferated after a hydrogel-soaked supernatant sample (diluted 10,000-fold) was applied to an LB agar plate. (All data points represent mean  $\pm$  standard deviation of three independent replicates. Statistics were derived using the two tailed *t*-test. \*\**P* < 0.01.)



model and performed morphological staining of the mouse femur slices at various time intervals. Hematoxylin and Eosin (H&E) and Safranin-O/Fast Green staining results indicated that the remodeling and mineralization processes of the cartilaginous callus were initiated at the early stage of endochondral ossification (Fig. S2). Moreover, recent

studies have revealed that serum nitric oxide levels are evidently elevated upon injury (for example, bone fracture), peaking at 14 days after human femoral fracture [35–38]. By monitoring the time-dependent changes in serum nitric oxide levels in the mouse femoral fracture model, we found out that the peak serum nitric oxide

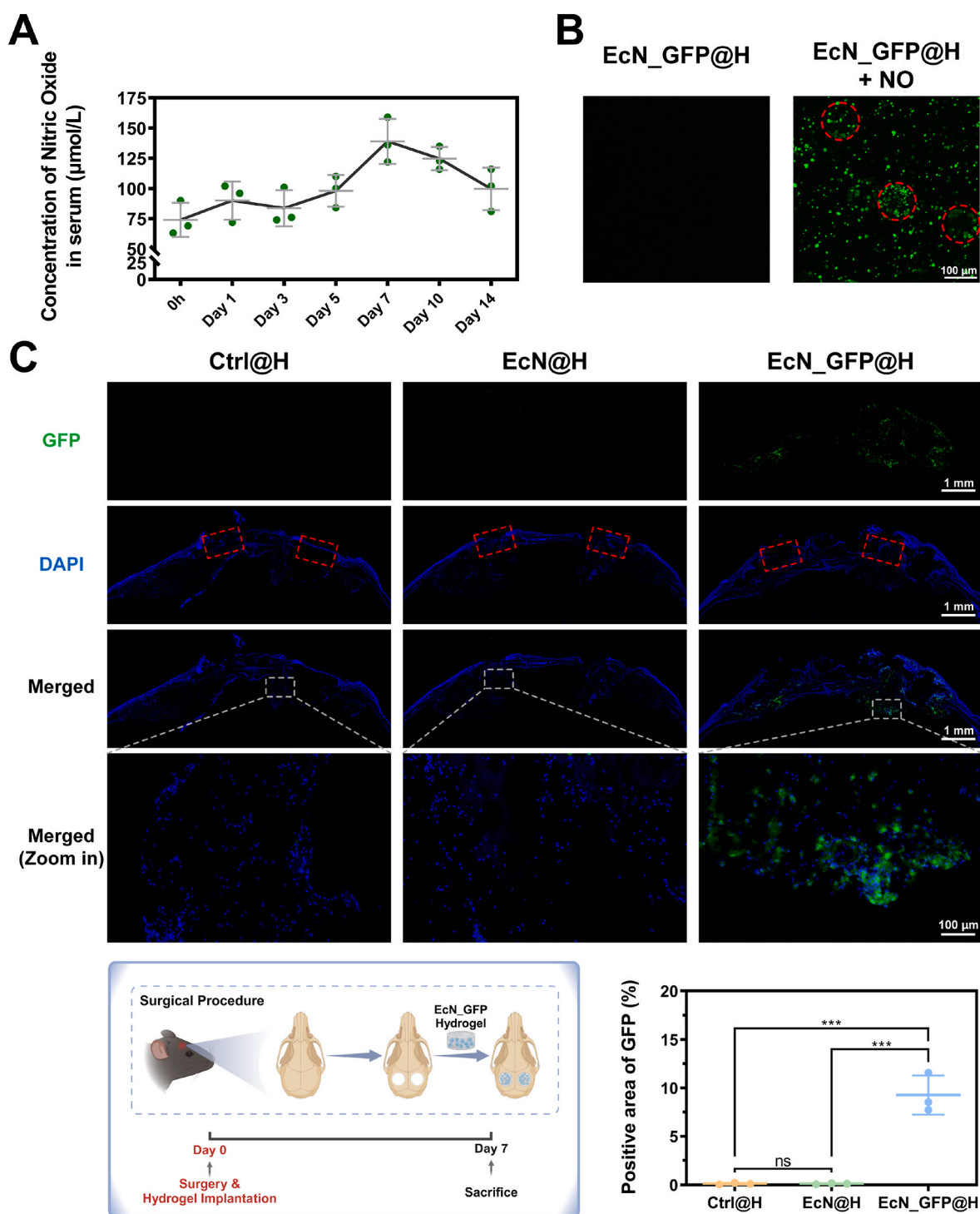


**Fig. 4.** The sensing-reporting capacity of the smart living hydrogel. (A) The time-dependent changes of serum nitric oxide levels in the mouse femoral fracture model. (All data points represent mean  $\pm$  standard deviation of three independent replicates at each time point.) (B) Fluorescence images of composite hydrogel in the presence or absence of nitric oxide. Red circles indicate EcN\_GFP encapsulated in the GelMA microspheres. (Scale bar: 100  $\mu\text{m}$ . EcN\_GFP@H: EcN\_GFP Hydrogel.) (C) Representative fluorescence images of the cranium slices of mouse cranial defect model in different groups on day 7. Red boxes indicated the original defected area. Gray boxes represented the specific location of the high magnification field. The illustration was created in BioRender by Fang, H. (2025). (Scale bar: 1 mm for low magnification fields and 100  $\mu\text{m}$  for high magnification fields. Ctrl@H: hydrogel control; EcN@H: Nissle 1917 hydrogel; EcN\_GFP@H: EcN\_GFP Hydrogel. All data points represent mean  $\pm$  standard deviation of three independent replicates. Statistics were derived using the one-way analysis of variance. \*\*\*P < 0.001.)

level emerged on day 7, which was in accordance with the ossification activities of fracture healing in mice (Fig. 4A).

To visualize the NO sensitivity of the smart living hydrogel, we constructed the pET22b-PnorVβ-norR-gfp plasmid and transformed it into EcN strain to generate EcN\_GFP strain, which was further encapsulated in the double-layered composite hydrogel system as described above (abbreviated as EcN\_GFP@H). Elevated NO in the microenvironment triggers norR-based regulatory circuits in EcN\_GFP and initiates the synthesis of GFP, thus signaling the presence of NO. EcN\_GFP@H exhibited green fluorescence in the presence of nitric oxide (1 mmol/L of DETA-NONOate as the NO donor), demonstrating the successful construction of the NO-responsive circuit and double-layered hydrogel structure (Fig. 4B). The *in vivo* NO sensitivity of the smart living hydrogel was further explored by implanting different groups of composite hydrogels in a mouse cranial defect model and performing fluorescence imaging of cranial slices on day 7. Fluorescent signals within the cranial defects in the EcN\_GFP@H group indicated NO enrichment in the defected area, which could be sensitively detected by the genetically engineered EcN (Fig. 4C). Moreover, the ELISA analysis of *in vitro* BMP2 release from EcN\_BMP2-encapsulated living hydrogels in the presence of NO donor also confirmed that the living hydrogel system provides sustained and controlled BMP2 release without compromising the biological activity of the encapsulated bacteria (Fig. S3).

### 3.4. Biocompatibility and osteoinductivity of the smart living hydrogel

To evaluate the biocompatibility of the genetically modified probiotics and smart living hydrogels, a set of cytotoxicity and viability experiments were conducted (Fig. 5A). After co-culture with the control Hydrogel (Ctrl@H), Nissle 1917 Hydrogel (EcN@H), and EcN\_BMP2 Hydrogel (mEcN@H) for different time intervals, the viability and proliferation of BMSCs were identified using CCK-8 and live/dead viability assays. There was no significant difference in the proliferation of each group, demonstrating the biocompatibility of EcN\_BMP2 and composite hydrogels (Fig. 5B and C). Notably, the presence of NO (1 mmol/L DETA-NONOate was added into the media in the mEcN@H + NO group) had no obvious inhibitory effects on the proliferation of BMSCs. Furthermore, the fluorescence images of the BMSC cytoskeleton indicated that different groups of hybrid hydrogels could well support cell attachment and help maintain normal cell morphology (Fig. 5D), which was not affected by the presence of NO as well. Considering the above results, we ascertained the biocompatibility of the genetically modified EcN and hybrid hydrogels *in vitro*.

After co-culture with different hydrogels for 14 days, alkaline phosphatase (ALP) staining of BMSCs was performed to manifest the difference in osteogenic ability between the groups (Fig. 5E). It was noted that the positive cell ratio of ALP staining in the mEcN@H + NO group reached  $48.82 \pm 2.57\%$ , which was significantly higher than that of the other groups, indicating that the EcN\_BMP2 could sensitively respond to the NO in the solution and subsequently synthesize BMP2 to facilitate osteogenic differentiation of BMSCs. Alizarin red staining (ARS) was conducted to visualize the formation of calcium nodules following a 21-day period of osteogenic induction, and expectedly the ARS results exhibited a similar trend to that of the ALP staining results (Fig. 5F). The expression levels of osteogenesis-related genes, including *BGLAP* (osteocalcin, *OCN*), *COL1A1* (collagen type I alpha 1), and *SPP1* (osteopontin, *OPN*), were detected using RT-qPCR (Fig. 5G). The semi-quantitative analysis demonstrated the highest expression of *BGLAP*, *COL1A1*, and *SPP1* in the mEcN@H + NO group (reaching  $2.79 \pm 0.05$  times,  $2.01 \pm 0.05$  times, and  $3.47 \pm 0.20$  times the expression level of the control group, respectively), indicating its osteoinductive potential. Additionally, the expression of these osteogenesis-associated genes was significantly enhanced in the mEcN@H + NO group, whereas the corresponding gene expression in the other groups was not significantly different from that in the control group. These results confirmed that, in

the presence of NO, the smart living hydrogel exhibited a superior promotive effect on the osteogenic differentiation of BMSCs, making it a promising candidate for bone regeneration.

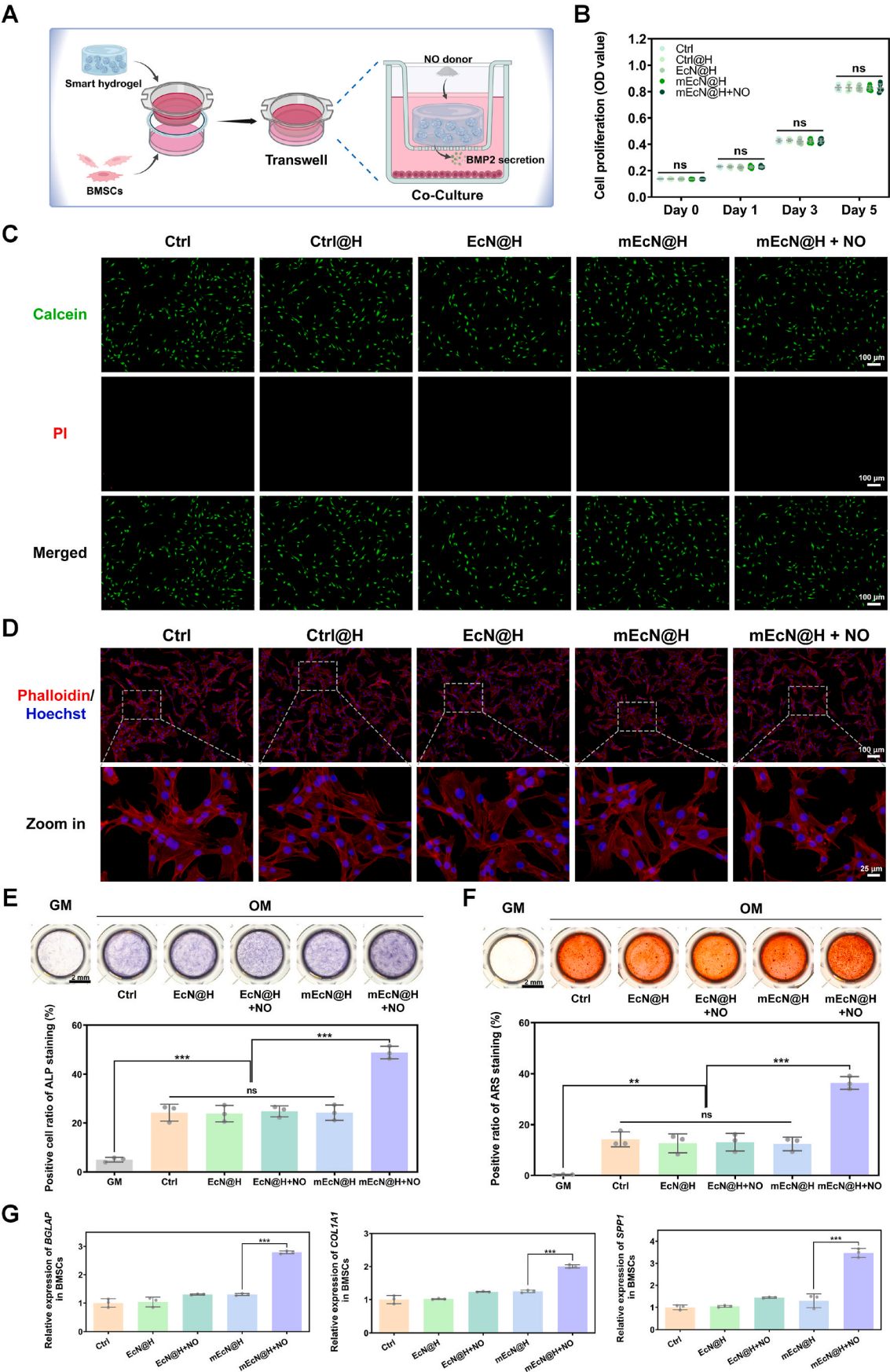
To further explore the *in vivo* biosafety of the smart living hybrid hydrogel, various biosafety assessments were conducted after the implantation of different hydrogels in a mouse femoral shaft fracture model and the mouse cranial defect model. Gross observation and H&E staining of the bone defects and major organs (that is, heart, liver, lung, spleen, kidney, and intestine) on day 28 showed no obvious inflammatory reaction or immunological response in any group (Figs. S4, S5, S6). Notably, the H&E staining results of the defect area at different time points indicated that the double-layer-embedment structure of the composite hydrogels in the EcN@H and mEcN@H groups managed to prevent the potential leakage of the probiotics in the early stage (that is, from day 1 to day 14), and the residues from probiotic apoptosis and hydrogel degradation did not trigger any *in situ* immune response at the later stage (that is, from day 14 to day 28) (Fig. S5). The mouse blood analysis results from each group, including the counts of white blood cells (WBC), red blood cells (RBC), hemoglobin (Hb), and red cell distribution width (RDW), were within the normal range and showed no significant difference between the groups (Fig. S7), ruling out the risk of any potential immune response, septicemia, or attack on the hematological system. The body weight of each group revealed no significant differences or sudden weight loss, in accordance with the above results (Fig. S8). In summary, these results demonstrated the superior histocompatibility and biosafety of the smart living hybrid hydrogel.

### 3.5. The living hydrogel promotes bone healing in femoral shaft fracture and cranial defect models

Bone formation and regeneration are complex events involving the coordination of diverse biological processes, which could be categorized as intramembranous and endochondral bone formation [46]. To comprehensively evaluate the *in vivo* therapeutic performance of the microenvironment-responsive living hydrogel, we utilized two well-established critical-sized bone defect models as the representatives of intramembranous ossification and endochondral ossification. Concretely, the mouse femoral shaft fracture model represents endochondral ossification of the femur, while the mouse cranial defect model represents intramembranous ossification of the cranium.

A mouse femoral shaft fracture model was established to evaluate the biocompatibility, osteoconductivity, and osteoinductivity of the smart living hydrogel during endochondral ossification (Fig. 6A and B). After femoral shaft fracture establishment and surgical implantation of different hydrogels, the mice were sacrificed at different time points (on day 14 and day 28 after surgery) for radiographic, morphological, and histological evaluation. Radiographs on day 14 revealed that the bone callus in the mEcN@H group were obviously more apparent than those in the other groups (Fig. 6C). Notably, the mice in the mEcN@H group almost reached fracture union on day 28, whereas evident callus and fracture lines could still be observed in the Ctrl@H and EcN@H groups (Fig. 6C). To further compare the quality and quantity of newly formed bones in different groups, we used the Mimics software to analyze the micro-CT data, which utilized pseudo-color labeling on the cross-sectional images of bone based on the differences in bone density (Fig. 6D). These images revealed that the quantity and density of newly formed bones in the mEcN@H group were superior to those in the other groups. For the quantitative assessment of fracture healing, essential parameters, including bone mineral density (BMD), trabecular bone volume fraction (BV/TV), trabecular number (Tb.N), and total porosity, were analyzed for each group (Fig. 6E). Significantly, the mEcN@H group exhibited a superior BMD ( $0.39 \pm 0.02 \text{ g/cm}^3$ ) with an evidently elevated BV/TV ratio ( $53.18 \pm 3.83\%$ ) and Tb.N ( $2.41 \pm 0.06/\text{mm}$ ), resulting in a relatively low total porosity ( $46.82 \pm 3.83\%$ ). In summary, these radiographic results indicated that the EcN\_BMP2 composite hydrogel could facilitate the mineralization of cartilage callus, and thus





(caption on next page)

**Fig. 5.** *In vitro* biocompatibility of the smart living hydrogel. (A) Illustration of *in vitro* co-culturing experiments. Created in BioRender by Fang, H. (2025). (B) Cell Counting Kit-8 assay of BMSCs treated with the indicated conditions. (All data points represent mean  $\pm$  standard deviation of six independent replicates. Statistics were derived using the two-way analysis of variance. ns: no significant difference.) (C) Live/dead viability assay of BMSCs treated with the indicated conditions for 2 days. BMSCs were stained with Calcein AM (live cells, green fluorescence) and PI (dead cells, red fluorescence). (Scale bar: 100  $\mu$ m) (D) Fluorescence images of BMSCs attachment and morphology after treatment with the indicated conditions for 2 days. BMSCs were stained with rhodamine phalloidin (cytoskeleton, red fluorescence) and Hoechst 33342 (cell nuclei, blue fluorescence). (Scale bar: 100  $\mu$ m for low magnification fields and 25  $\mu$ m for high magnification fields.) (E) The ALP staining of BMSCs after treatment with osteogenic differentiation medium for 14 days under indicated conditions. The representative and quantitative results of staining for different groups were shown in the figure. (Scale bar: 2 mm. All data points represent mean  $\pm$  standard deviation of three independent replicates. Statistics were derived using the one-way analysis of variance. \*\*\* $P < 0.001$ .) (GM: growth media, OM: osteogenic media, EcN@H: co-cultured with Nissle 1917 Hydrogel, mEcN@H: co-cultured with NO-BMP2@Nissle 1917 Hydrogel, NO: addition of 1 mmol/L DETA-NONoate in the media) (F) The ARS staining of BMSCs after treatment with osteogenic differentiation medium for 21 days under indicated conditions. The representative and quantitative results of staining for different groups were shown in the figure. (Scale bar: 2 mm. All data points represent mean  $\pm$  standard deviation of three independent replicates. Statistics were derived using the one-way analysis of variance. \*\* $P < 0.01$ , \*\*\* $P < 0.001$ .) (G) The expression level of osteogenesis-associated genes in BMSCs after treatment with the indicated conditions for 7 days. (All data points represent mean  $\pm$  standard deviation of three independent replicates. Statistics were derived using the one-way analysis of variance. \*\*\* $P < 0.001$ .)

accelerate the healing process of femoral fracture.

Furthermore, morphological and immunohistochemical staining were utilized to analyze and compare certain components of the callus in different groups (Fig. 6F). Safranin-O/Fast Green staining, which was commonly applied to distinguish cartilage tissues (stained as red) from bone tissues (stained as green), demonstrated that the proportion of cartilage components in the callus of mEcN@H group at day 14 ( $14.26 \pm 1.75\%$ ) was significantly lower than that of Ctrl@H group and EcN@H group ( $39.96 \pm 1.65\%$  and  $38.90 \pm 5.12\%$ , respectively), indicating that the ossification process of soft callus was more advanced in mEcN@H group. Correspondingly, the proportion of trabecular and cortical bone within the callus in mEcN@H group reached  $37.45 \pm 2.20\%$  at day 14 and  $51.79 \pm 3.56\%$  at day 28, which was evidently higher than those of the other groups throughout the fracture healing process. Moreover, the secretion and deposition of collagen type 1 (COL1), one of the most important bone matrix components in mature bone tissue, in the bone callus of the mEcN@H group was significantly promoted on day 14 and day 28 (Fig. 6F). These results verified that the EcN\_BMP2 composite hydrogel could sensitively respond to the elevated NO concentration at the fracture site and subsequently secrete BMP2, accelerating cartilage calcification and promoting the secretion and deposition of COL1 in the callus. Moreover, upregulated expression of osteogenesis-associated markers, including BMP2 and Runt-related transcription factor 2 (RUNX2), was observed in the immunohistochemical staining of the mEcN@H group on both day 14 and 28, revealing the robust osteogenic efficacy of the NO-responsive living hydrogel (Fig. S9).

Hypertrophic chondrocytes modulate endochondral bone formation by secreting matrix metalloproteinase 13 (MMP13) to degrade the cartilage matrix, secreting vascular endothelial growth factor (VEGF) to guide vascularization, and undergoing osteogenic transdifferentiation under neovascular stimulation [47,48]. Significantly, the expression level of MMP13 in the callus of the mEcN@H group was higher than that in the other groups on day 14, indicating an elevated functionality level of the hypertrophic chondrocytes (Fig. S10). Considering that the coupling of vascularization and osteogenesis is the basis for bone remodeling, the expression levels of CD31, which is widely expressed at the intercellular junctions of vascular endothelial cells and is highly expressed in H-type vascular endothelial cells in bone tissues [49], were explored in different groups (Fig. 6F). The expression of CD31 in the callus of the mEcN@H group was significantly higher than that of the other groups throughout the healing process. Concretely, the expression level of CD31 in mEcN@H group reached  $14.46 \pm 3.10\%$  on day 14 (nearly triple the level of every other group), demonstrating that vascularization was more advanced in the mEcN@H group during the early stage of callus ossification, thereby promoting endochondral bone formation. In summary, the immunohistochemical staining of MMP13 and CD31 led us to infer that BMP2 secretion from the EcN\_BMP2 composite hydrogel could facilitate the function and transdifferentiation of hypertrophic chondrocytes, which in turn promoted the secretion of VEGF for vascularization and accelerated subsequent callus remodeling.

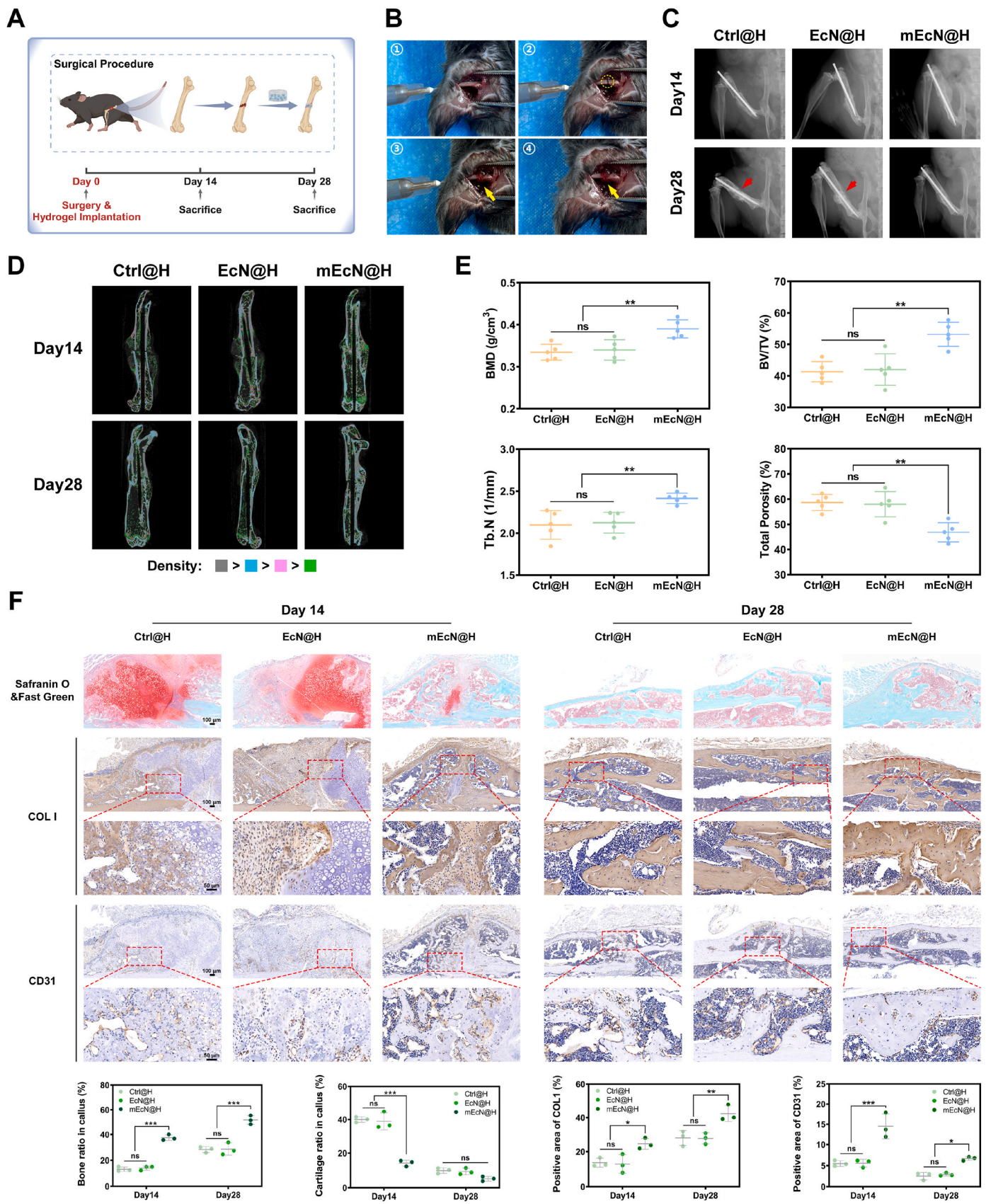
To further evaluate the performance of the living hybrid hydrogel during intramembranous ossification, a mouse model with cranial defects was used (Fig. S11). After the surgical implantation of different hydrogels, the mice were sacrificed at different time points (on day 14 and day 28 after surgery) for radiographic, morphological, and histological evaluation. 3D reconstruction of the harvested craniums and quantitative assessment results (that is, BMD, BV/TV, Tb.N, and total porosity) revealed a higher percentage of newly formed bone tissue volume within the defect area in the mEcN@H group, indicating that the EcN\_BMP2 composite hydrogel could facilitate the process of intramembranous ossification (Fig. S12A and S12B). The proportion of cartilage components in the newly formed cranium was low in each group throughout the bone regeneration process, in accordance with the physiological remodeling process of intramembranous ossification (Fig. S13). In contrast, the proportion of trabecular and cortical bone in the defect area in the mEcN@H group was higher than that in other groups. Notably, the expression level of Runt-related transcription factor 2 (RUNX2), a typical marker of intramembranous ossification [50], was significantly higher in the mEcN@H group than that in the other groups on both day 14 and day 28 (Fig. S13). We also observed that the expression levels of VEGF and CD31 in the mEcN@H group were evidently higher than those in the other groups throughout the regeneration process (Fig. S13), indicating more prominent angiogenic activity and more extensive vascular distribution, thus facilitating intramembranous ossification. In summary, these results indicated that EcN\_BMP2 can sensitively detect the nitric oxide in the microenvironment and induce BMP2 synthesis and secretion, thereby facilitating osteogenic differentiation and vascularization during intramembranous ossification.

#### 4. Conclusion and discussion

Significant progress has been made in addressing the growing demand for precise interventions and treatments for bone fractures. Representative examples include photo- or thermo-responsive hydrogels incorporating BMP2-functionalized nanosheets to achieve precise and sustained release [51,52], and sophisticated nanostructures engineered to enhance the efficacy of pre-loaded BMP2 release [53–55]. None of these approaches endowed the biomaterials with a self-activating quality or microenvironmental responsiveness, as they often lacked the design consideration of addressing continuous microenvironmental changes in bone defects or fractures and failed to provide self-corrected doses of therapeutics during the regeneration processes.

Hydrogel scaffolds have attracted increasing attention within the field of bone tissue engineering as drug and cell delivery vehicles owing to their unique properties compared with inorganic materials, including higher cell affinity, balanced mechanical properties, and remarkable degradability [11,19,56,57]. In this study, we developed an innovative Living Responsive Regenerative Medicine (LRRM) system based on a living hydrogel device for the treatment of bone fractures and





(caption on next page)

**Fig. 6.** The smart living hydrogel promotes bone healing of femoral shaft fracture. (A) The schematic diagram of the femoral shaft fracture model. Created in BioRender by Fang, H. (2025). (B) Intraoperative photograph during the modeling process of femoral shaft fracture. The yellow circle and arrows indicated the fracture line. (C) Radiographic imaging of femurs at different time points. Red arrows indicated that the fracture line was more evident in Ctrl@H and EcN@H group at day 28. (D) Representative Mimics pseudo color labeling on the cross-sectional images of femurs. (Bone density: gray area > blue area > red area > green area) (E) Micro-CT analysis of callus area at day 28. The bone mineral density (BMD), trabecular bone volume fraction (BV/TV), trabecular number (Tb.N) and total porosity were measured from the Micro-CT data. (All data points represent mean  $\pm$  standard deviation of five independent replicates. Statistics were derived using the one-way analysis of variance. \* $P < 0.05$ , \*\* $P < 0.01$ , \*\*\* $P < 0.001$ ) (F) Morphological staining (Safranin-O/Fast Green) and immunohistochemical staining (COL 1, CD31) of femur slicing of different groups. The red boxes represented the specific location of the high magnification field. (Scale bar: 100  $\mu$ m for low magnification fields and 50  $\mu$ m for high magnification fields.) The quantitative results of morphological staining and immunohistochemical staining for different groups at each time point were shown in the figure. (All data points represent mean  $\pm$  standard deviation of three independent replicates. Statistics were derived using the two-way analysis of variance. \* $P < 0.05$ , \*\* $P < 0.01$ , \*\*\* $P < 0.001$ .)

critical-sized bone defects. By transfecting EcN with the recombinant pET22b-PnorV $\beta$ -norR-NSP4-bmp2 plasmid, we engineered a therapeutic probiotic capable of responding to NO fluctuations in the microenvironment (for example, at the fracture site or the bone defect area). This engineered probiotic initiated an NO-induced circuit for the real-time synthesis and secretion of BMP2, thereby facilitating fracture healing and bone regeneration in a self-activating and microenvironment-responsive manner. Unlike static delivery systems [58,59], this LRRM system enables dynamic and self-regulating BMP2 release in response to microenvironmental NO fluctuations, which avoids burst release and ensures sustained, on-demand therapy. Additionally, EcN's genetic programmability allows future integration of multi-factor delivery, such as VEGF + BMP2, surpassing the limitations of single-factor approaches. In the practical application of our LRRM system, engineered probiotics underwent encapsulation in the GelMA hydrogel microspheres followed by the embedment in a bulky HAMA hydrogel network, resulting in a double-layered living hydrogel system. Hydrogel encapsulation serves a dual purpose: it provides an optimal porous framework that fosters bacterial proliferation while concurrently acting as a containment barrier, thereby mitigating the unintentional leakage of viable bacteria into the surrounding environment. Importantly, in contrast to traditional strategies, our LRRM system allows real-time synthesis and secretion of BMP2 without burst release or rapid *in vivo* degradation. This innovative approach offers superior therapeutic outcomes compared with conventional controlled-release systems.

Considering that diverse natural biological signal-response systems are ripe for engineering, as well as the genetically engineerable feature of our LRRM system, we envision its potential as a versatile agent that can be synergistically combined with other modalities to achieve applications beyond bone tissue regeneration. For example, the application scenarios of the LRRM system may encompass a spectrum of therapeutic areas, including anti-tumor, anti-inflammatory, anti-infection therapies. Notably, within this innovative biological signal-response system, the *cargo* (genetically engineered probiotics) and the *vehicle* (bilayer-structured encapsulation-releasing system) can be tailored and interchanged, enabling enhanced capabilities, such as sensing and reporting on diverse biological signals. This flexibility allows for the on-demand release of multiple factors in a precisely controlled manner, offering temporal and spatial advantages.

Despite these potential merits, several challenges must be surmounted to fully exploit the clinical applications of LRRM, including navigating the intricate microenvironment of human tissues, mitigating the risk of bacterial leakage, and optimizing the mechanical properties of biomaterials. We envision that the LRRM system will guide future efforts for automated *in vivo* drug delivery, significantly improving its suitability for clinical translation and serving as a promising strategy for developing safe and effective therapies for skeletal and other diseases.

#### CRedit authorship contribution statement

**Haoyu Fang:** Writing – review & editing, Writing – original draft, Visualization, Project administration, Methodology, Investigation, Funding acquisition, Formal analysis, Data curation, Conceptualization. **Yanyi Wang:** Writing – review & editing, Writing – original draft,

Visualization, Methodology, Investigation, Funding acquisition, Formal analysis, Data curation, Conceptualization. **Li Li:** Writing – original draft, Visualization, Methodology, Investigation, Formal analysis. **Xiaotong Qin:** Writing – review & editing, Validation, Methodology, Investigation. **Daoyu Zhu:** Writing – review & editing, Methodology, Investigation, Data curation. **Pei Liu:** Writing – review & editing, Validation, Methodology. **Qianhao Yang:** Writing – review & editing, Validation, Methodology. **Youshui Gao:** Writing – review & editing, Validation, Investigation, Data curation. **Zhongmin Shi:** Writing – review & editing, Validation. **Xin Ma:** Writing – review & editing, Validation, Conceptualization. **Chao Zhong:** Writing – review & editing, Validation, Supervision, Project administration, Funding acquisition, Conceptualization. **Yixuan Chen:** Writing – review & editing, Validation, Supervision, Project administration, Funding acquisition, Conceptualization.

#### 5. Ethics approval and consent to participate

All procedures for the care and use of laboratory animals were approved by the Animal Research Committee of Shanghai Sixth People's Hospital Affiliated to Shanghai Jiao Tong University School of Medicine (No. 2023–0204). All animal housing and experiments were conducted in strict accordance with the institutional Guidelines for Care and Use of Laboratory Animals at Shanghai Sixth People's Hospital Affiliated to Shanghai Jiao Tong University School of Medicine.

#### Data availability

The datasets that support the findings of this study are available on request from the corresponding authors.

#### Declaration of competing interest

The authors declare that they have no known competing financial interests or personal relationships that could have appeared to influence the work reported in this paper.

#### Acknowledgements

H. Fang and Y. Wang are co-first authors and contributed equally to this work. This project was funded by the National Natural Science Foundation of China, China (Grant No. 81902237, 32201202), the National Key R&D Program of China, China (Grant No. 2020YFA0908100), the National Science Fund for Distinguished Young Scholars, China (Grant No. 32125023), the Shenzhen Science and Technology Program, China (Grant No. ZDSYS20220606100606013) and the China Postdoctoral Science Foundation, China (Grant No. 2023M742324). The schematic illustrations in Figs. 4C, 5A, 6A, and Fig. S11A were created with BioRender.com.

#### Appendix A. Supplementary data

Supplementary data to this article can be found online at <https://doi.org/10.1016/j.bioactmat.2025.04.020>.



## References

- [1] H.W. Kang, S.J. Lee, I.K. Ko, C. Kengla, J.J. Yoo, A. Atala, A 3D bioprinting system to produce human-scale tissue constructs with structural integrity, *Nat. Biotechnol.* 34 (3) (2016) 312–319, <https://doi.org/10.1038/nbt.3413>.
- [2] A.K. Gaharwar, I. Singh, A. Khademhosseini, Engineered biomaterials for in situ tissue regeneration, *Nat. Rev. Mater.* 5 (9) (2020) 686–705, <https://doi.org/10.1038/s41578-020-0209-x>.
- [3] H. Ravanbakhsh, V. Karamzadeh, G. Bao, L. Mongeau, D. Juncker, Y.S. Zhang, Emerging technologies in multi-material bioprinting, *Adv. Mater.* 33 (49) (2021) e2104730, <https://doi.org/10.1002/adma.202104730>.
- [4] H. Fang, D. Zhu, Q. Yang, Y. Chen, C. Zhang, J. Gao, Y. Gao, Emerging zero-dimensional to four-dimensional biomaterials for bone regeneration, *J. Nanobiotechnol.* 20 (1) (2022) 26, <https://doi.org/10.1186/s12951-021-01228-1>.
- [5] P. Lu, D. Ruan, M. Huang, M. Tian, K. Zhu, Z. Gan, Z. Xiao, Harnessing the potential of hydrogels for advanced therapeutic applications: current achievements and future directions, *Signal Transduct. Targeted Ther.* 9 (1) (2024) 166, <https://doi.org/10.1038/s41392-024-01852-x>.
- [6] G.L. Koons, M. Diba, A.G. Mikos, Materials design for bone-tissue engineering, *Nat. Rev. Mater.* 5 (8) (2020) 584–603, <https://doi.org/10.1038/s41578-020-0204-2>.
- [7] C. Wang, E.S. Sani, C.D. Shih, C.T. Lim, J. Wang, D.G. Armstrong, W. Gao, Wound management materials and technologies from bench to bedside and beyond, *Nat. Rev. Mater.* 9 (2024) 550–566, <https://doi.org/10.1038/s41578-024-00693-y>.
- [8] A. Pamela Silver, T. David Rigrler, Engineering bacteria for diagnostic and therapeutic applications, *Nat. Rev. Microbiol.* 16 (4) (2018) 214–225, <https://doi.org/10.1038/nrmicro.2017.172>.
- [9] T.C. Tang, B. An, Y. Huang, S. Vasikaran, Y. Wang, X. Jiang, T.K. Lu, C. Zhong, Materials design by synthetic biology, *Nat. Rev. Mater.* 6 (4) (2021) 332–350, <https://doi.org/10.1038/s41578-020-00265-w>.
- [10] A. Rodrigo-Navarro, S. Sankaran, M.J. Dalby, A. del Campo, M. Salmeron-Sanchez, Engineered living biomaterials, *Nat. Rev. Mater.* 6 (12) (2021) 1175–1190, <https://doi.org/10.1038/s41578-021-00350-8>.
- [11] X. Liu, M.E. Inda, Y. Lai, T.K. Lu, X. Zhao, Engineered living hydrogels, *Adv. Mater.* 34 (26) (2022) e2201326, <https://doi.org/10.1002/adma.202201326>.
- [12] P. Praveschotinunt, A.M. Duraj-Thatte, I. Gelfat, F. Bahl, N.S. Joshi, Engineered E. coli Nissle 1917 for the delivery of matrix-tethered therapeutic domains to the gut, *Nat. Commun.* 10 (1) (2019) 5580, <https://doi.org/10.1038/s41467-019-13336-6>.
- [13] J.J. Hay, A. Rodrigo-Navarro, M. Petaroudi, A.V. Bryksin, A.J. García, T.H. Barker, M.J. Dalby, M. Salmeron-Sanchez, Bacteria-based materials for stem cell engineering, *Adv. Mater.* 30 (43) (2018) 1804310, <https://doi.org/10.1002/adma.201804310>.
- [14] B.M. Scott, C. Gutiérrez-Vázquez, L.M. Sanmarco, J.A.D.S. Pereira, F.J. Quintana, Self-tunable engineered yeast probiotics for the treatment of inflammatory bowel disease, *Nat. Med.* 27 (7) (2021) 1212–1222, <https://doi.org/10.1038/s41591-021-01390-x>.
- [15] A. Courbet, D. Endy, E. Renard, F. Molina, J. Bonnet, Detection of pathological biomarkers in human clinical samples via amplifying genetic switches and logic gates, *Sci. Transl. Med.* 7 (289) (2015), <https://doi.org/10.1126/scitranslmed.aaa3601>, 289ra83.
- [16] M. Mimeo, P. Nadeau, A. Hayward, S. Carim, S. Flanagan, L. Jerger, J. Collins, S. McDonnell, R. Swartwout, R.J. Citorik, V. Bulovic, R. Langer, G. Traverso, A. P. Chandrakasan, T.K. Lu, An ingestible bacterial-electronic system to monitor gastrointestinal health, *Science* 360 (6391) (2018) 915–918, <https://doi.org/10.1126/science.aas9315>.
- [17] D.T. Rigrler, T.W. Giessen, M. Baym, S.J. Kerns, M.J. Niederhuber, R.T. Bronson, J. W. Kotula, G.K. Gerber, J.C. Way, P.A. Silver, Engineered bacteria can function in the mammalian gut long-term as live diagnostics of inflammation, *Nat. Biotechnol.* 35 (7) (2017) 653–658, <https://doi.org/10.1038/nbt.3879>.
- [18] M.E. Inda-Webb, M. Jimenez, Q. Liu, N.V. Phan, J. Ahn, C. Steiger, A. Wentworth, A. Riaz, T. Zirtiloglu, K. Wong, K. Ishida, N. Fabian, J. Jenkins, J. Kuosmanen, W. Madani, R. McNally, Y. Lai, A. Hayward, M. Mimeo, P. Nadeau, A. P. Chandrakasan, G. Traverso, R.T. Yazicigil, T.K. Lu, Sub-1.4 cm(3) capsule for detecting labile inflammatory biomarkers in situ, *Nature* 620 (7973) (2023) 386–392, <https://doi.org/10.1038/s41586-023-06369-x>.
- [19] Y. Lu, H. Li, J. Wang, M. Yao, Y. Peng, T. Liu, Z. Li, G. Luo, J. Deng, Engineering bacteria-activated multifunctionalized hydrogel for promoting diabetic wound healing, *Adv. Funct. Mater.* 31 (48) (2021) 2105749, <https://doi.org/10.1002/adfm.202105749>.
- [20] C. Loong, H. Qing, Chua, K. Jiew, Aram Kang, K. Hon, Ling, K. Lin, W. Shan, Engineered commensal microbes for diet-mediated colorectal-cancer chemoprevention, *Nat. Biomed. Eng.* 2 (1) (2018) 27–37, <https://doi.org/10.1038/s41551-017-0181-y>.
- [21] Z.P. Zou, Y. Du, T.T. Fang, Y. Zhou, B.C. Ye, Biomarker-responsive engineered probiotic diagnoses, records, and ameliorates inflammatory bowel disease in mice, *Cell Host Microbe* 31 (2) (2023) 199–212.e5, <https://doi.org/10.1016/j.chom.2022.12.004>.
- [22] S. Vermeulen, Z. Tahmasebi Birgani, P. Habibovic, Biomaterial-induced pathway modulation for bone regeneration, *Biomaterials* 283 (2022) 121431, <https://doi.org/10.1016/j.biomaterials.2022.121431>.
- [23] D.M. Ibrahim, A. Fomina, C.V.C. Bouten, A. Smits, Functional regeneration at the blood-biomaterial interface, *Adv. Drug Deliv. Rev.* 201 (2023) 115085, <https://doi.org/10.1016/j.addr.2023.115085>.
- [24] D. Khare, B. Basu, A.K. Dubey, Electrical stimulation and piezoelectric biomaterials for bone tissue engineering applications, *Biomaterials* 258 (2020) 120280, <https://doi.org/10.1016/j.biomaterials.2020.120280>.
- [25] Y. Chen, J. Yu, Q. Ke, Y. Gao, C. Zhang, Y. Guo, Bioinspired fabrication of carbonated hydroxyapatite/chitosan nanohybrid scaffolds loaded with TWS119 for bone regeneration, *Chem. Eng. J.* 341 (2018) 112–125, <https://doi.org/10.1016/j.cej.2018.02.010>.
- [26] V.S. Salazar, L.W. Gamer, V. Rosen, BMP signalling in skeletal development, disease and repair, *Nat. Rev. Endocrinol.* 12 (4) (2016) 203–221, <https://doi.org/10.1038/nrendo.2016.12>.
- [27] Z. Yang, X. Li, X. Gan, M. Wei, C. Wang, G. Yang, Y. Zhao, Z. Zhu, Z. Wang, Hydrogel armed with Bmp2 mRNA-enriched exosomes enhances bone regeneration, *J. Nanobiotechnol.* 21 (1) (2023) 119, <https://doi.org/10.1186/s12951-023-01871-w>.
- [28] A.M. McDermott, S. Herberg, D.E. Mason, J.M. Collins, H.B. Pearson, J. H. Dawahare, R. Tang, A.N. Patwa, M.W. Grinstaff, D.J. Kelly, E. Alsberg, J. D. Boerckel, Recapitulating bone development through engineered mesenchymal condensations and mechanical cues for tissue regeneration, *Sci. Transl. Med.* 11 (495) (2019), <https://doi.org/10.1126/scitranslmed.aav7756> eav7756.
- [29] B. Prados, R. Del Toro, D. MacGrogan, P. Gómez-Apiñániz, T. Papoutsis, P. Muñoz-Cánoves, S. Méndez-Ferrer, J.L. de la Pompa, Heterotopic ossification in mice overexpressing Bmp2 in Tie2+ lineages, *Cell Death Discov.* 12 (8) (2021) 729, <https://doi.org/10.1038/s41419-021-04003-0>.
- [30] J. Dong, X. Xu, Q. Zhang, Z. Yuan, B. Tan, Critical implication of the PTEN/PI3K/AKT pathway during BMP2-induced heterotopic ossification, *Mol. Med. Rep.* 23 (4) (2021) 254, <https://doi.org/10.3892/mmr.2021.11893>.
- [31] J. Fan, X. Zhang, M. Kang, C.S. Lee, L. Kim, D. Hadaya, T.L. Aghaloo, M. Lee, Complementary modulation of BMP signaling improves bone healing efficiency, *Biomaterials* 302 (2023) 122335, <https://doi.org/10.1016/j.biomaterials.2023.122335>.
- [32] H. Husanie, M. Abu-Remaih, K. Maroun, L. Abu-Tair, H. Safadi, K. Atlán, T. Golan, R.I. Aqeilan, Loss of tumor suppressor WWOX accelerates pancreatic cancer development through promotion of TGFβ/BMP2 signaling, *Cell Death Discov.* 13 (12) (2022) 1074, <https://doi.org/10.1038/s41419-022-05519-9>.
- [33] F. Huang, Y. Cao, C. Wang, R. Lan, B. Wu, X. Xie, J. Hong, L. Fu, G. Wu, PNMA5 promotes bone metastasis of non-small-cell lung cancer as a target of BMP2 signaling, *Front. Cell Dev. Biol.* 9 (2021) 678931, <https://doi.org/10.3389/fcell.2021.678931>.
- [34] Z.J. Gunderson, Z.R. Campbell, T.O. McKinley, R.M. Natoli, M.A. Kacena, A comprehensive review of mouse diaphyseal femur fracture models, *Injury* 51 (7) (2020) 1439–1447, <https://doi.org/10.1016/j.injury.2020.04.011>.
- [35] W. Zhu, A.D. Diwan, J.H. Lin, G.A. Murrell, Nitric oxide synthase isoforms during fracture healing, *J. Bone Miner. Res.* 16 (3) (2001) 535–540, <https://doi.org/10.1359/jbmr.2001.16.3.535>.
- [36] W. Zhu, G.A. Murrell, J. Lin, E.M. Gardiner, A.D. Diwan, Localization of nitric oxide synthases during fracture healing, *J. Bone Miner. Res.* 17 (8) (2002) 1470–1477, <https://doi.org/10.1359/jbmr.2002.17.8.1470>.
- [37] D. Keskin, A. Kiziltunç, Time-dependent changes in serum nitric oxide levels after long bone fracture, *Tohoku J. Exp. Med.* 213 (4) (2007) 283–289, <https://doi.org/10.1620/tjem.213.283>.
- [38] L.A. Ridnour, J.S. Isenberg, M.G. Espey, D.D. Thomas, D.D. Roberts, D.A. Wink, Nitric oxide regulates angiogenesis through a functional switch involving thrombospondin-1, *Proc. Natl. Acad. Sci. U. S. A.* 102 (37) (2005) 13147–13152, <https://doi.org/10.1073/pnas.0502979102>.
- [39] C. Differ, F. Klatte-Schulz, N. Bormann, S. Minkwitz, P. Knaus, B. Wildemann, Is NO the answer? The nitric oxide pathway can support bone morphogenetic protein 2 mediated signaling, *Cells* 8 (10) (2019) 1273, <https://doi.org/10.3390/cells8101273>.
- [40] D. Zhu, H. Fang, H. Yu, P. Liu, Q. Yang, P. Luo, C. Zhang, Y. Gao, Y.X. Chen, Alcohol-induced inhibition of bone formation and neovascularization contributes to the failure of fracture healing via the miR-19a-3p/FOXF2 axis, *Bone Joint Res* 11 (6) (2022) 386–397, <https://doi.org/10.1302/2046-3758.116.Bjr-2021-0596.R1>.
- [41] X. Chen, B. Wang, I. Thompson, W. Huang, Rational design and characterization of nitric oxide biosensors in E. coli Nissle 1917 and mini SimCells, *ACS Synth. Biol.* 10 (10) (2021) 2566–2578, <https://doi.org/10.1021/acssynbio.1c00223>.
- [42] K. Tsuji, A. Bandyopadhyay, B.D. Harfe, K. Cox, S. Kakar, L. Gerstenfeld, T. Einhorn, C.J. Tabin, V. Rosen, BMP2 activity, although dispensable for bone formation, is required for the initiation of fracture healing, *Nat. Genet.* 38 (12) (2006) 1424–1429, <https://doi.org/10.1038/ng1916>.
- [43] Z. Ming, L. Han, M. Bao, H. Zhu, S. Qiang, S. Xue, W. Liu, Living bacterial hydrogels for accelerated infected wound healing, *Adv. Sci.* 8 (24) (2021) e2102545, <https://doi.org/10.1002/adv.202102545>.
- [44] T.A. Einhorn, L.C. Gerstenfeld, Fracture healing: mechanisms and interventions, *Nat. Rev. Rheumatol.* 11 (1) (2015) 45–54, <https://doi.org/10.1038/nrrheum.2014.164>.
- [45] Z. Li, C.A. Meyers, L. Chang, S. Lee, Z. Li, R. Tomlinson, A. Hoke, T.L. Clemens, A. W. James, Fracture repair requires TrkA signaling by skeletal sensory nerves, *J. Clin. Invest.* 129 (12) (2019) 5137–5150, <https://doi.org/10.1172/JCI128428>.
- [46] L. Claes, S. Recknagel, A. Ignatius, Fracture healing under healthy and inflammatory conditions, *Nat. Rev. Rheumatol.* 8 (3) (2012) 133–143, <https://doi.org/10.1038/nrrheum.2012.1>.
- [47] S.A. Hallett, W. Ono, N. Ono, The hypertrophic chondrocyte: to be or not to be, *Histol. Histopathology (Oxf.)* 36 (10) (2021) 1021–1036, <https://doi.org/10.14670/hh-18-355>.
- [48] L. Yang, K.Y. Tsang, H.C. Tang, D. Chan, K.S.E. Cheah, Hypertrophic chondrocytes can become osteoblasts and osteocytes in endochondral bone formation, *Proc. Natl. Acad. Sci. U. S. A.* 111 (33) (2014) 12097–12102, <https://doi.org/10.1073/pnas.1302703111>.



- [49] A.P. Kusumbe, S.K. Ramasamy, R.H. Adams, Coupling of angiogenesis and osteogenesis by a specific vessel subtype in bone, *Nature* 507 (7492) (2014) 323–328, <https://doi.org/10.1038/nature13145>.
- [50] T. Komori, Runx2, an inducer of osteoblast and chondrocyte differentiation, *Histochem. Cell Biol.* 149 (4) (2018) 313–323, <https://doi.org/10.1007/s00418-018-1640-6>.
- [51] Z. Lv, T. Hu, Y. Bian, G. Wang, Z. Wu, H. Li, X. Liu, S. Yang, C. Tan, R. Liang, X. Weng, A MgFe-LDH nanosheet-incorporated smart thermo-responsive hydrogel with controllable growth factor releasing capability for bone regeneration, *Adv. Mater.* 35 (5) (2023) e2206545, <https://doi.org/10.1002/adma.202206545>.
- [52] W. Wang, G. Zhang, Y. Wang, J. Ran, L. Chen, Z. Wei, H. Zou, Y. Cai, W. Han, An injectable and thermosensitive hydrogel with nano-aided NIR-II phototherapeutic and chemical effects for periodontal antibacteria and bone regeneration, *J. Nanobiotechnol.* 21 (1) (2023) 367, <https://doi.org/10.1186/s12951-023-02124-6>.
- [53] G. Cheng, C. Yin, H. Tu, S. Jiang, Q. Wang, X. Zhou, X. Xing, C. Xie, X. Shi, Y. Du, H. Deng, Z. Li, Controlled co-delivery of growth factors through layer-by-layer assembly of core-shell nanofibers for improving bone regeneration, *ACS Nano* 13 (6) (2019) 6372–6382, <https://doi.org/10.1021/acsnano.8b06032>.
- [54] Y.H. Kim, Y. Tabata, Dual-controlled release system of drugs for bone regeneration, *Adv. Drug Deliv. Rev.* 94 (2015) 28–40, <https://doi.org/10.1016/j.addr.2015.06.003>.
- [55] M.T. Howard, S. Wang, A.G. Berger, J.R. Martin, S. Jalili-Firoozinezhad, R. F. Padera, P.T. Hammond, Sustained release of BMP-2 using self-assembled layer-by-layer film-coated implants enhances bone regeneration over burst release, *Biomaterials* 288 (2022) 121721, <https://doi.org/10.1016/j.biomaterials.2022.121721>.
- [56] G. Chen, F. Wang, X. Zhang, Y. Shang, Y. Zhao, Living microecological hydrogels for wound healing, *Sci. Adv.* 9 (21) (2023) eadg3478, <https://doi.org/10.1126/sciadv.adg3478>.
- [57] C. Zhang, Z.Y. Han, K.W. Chen, Y.Z. Wang, P. Bao, P. Ji, X. Yan, Z.Y. Rao, X. Zeng, X.Z. Zhang, In situ formed microalgae-integrated living hydrogel for enhanced tumor starvation therapy and immunotherapy through photosynthetic oxygenation, *Nano Lett.* 24 (12) (2024) 3801–3810, <https://doi.org/10.1021/acs.nanolett.4c00471>.
- [58] J. Deng, Y.Y. Tang, Q. Zhang, C. Wang, M. Liao, P. Ji, J.L. Song, G.X. Luo, L. Chen, X.H. Ran, Z.M. Wei, L.W. Zheng, R.Y. Dang, X. Liu, H.M. Zhang, Y.S. Zhang, X. M. Zhang, H. Tan, A bioinspired medical adhesive derived from skin secretion of *Andrias davidianus* for wound healing, *Adv. Funct. Mater.* 29 (31) (2019) 1809110, <https://doi.org/10.1002/adfm.201809110>.
- [59] S. Wang, C. Yan, X. Zhang, D. Shi, L. Chi, G. Luo, J. Deng, Antimicrobial peptide modification enhances the gene delivery and bactericidal efficiency of gold nanoparticles for accelerating diabetic wound healing, *Biomater. Sci.* 6 (10) (2018) 2757–2772, <https://doi.org/10.1039/c8bm00807h>.